Separation and Purification Technology 230 (2020) 115877

Contents lists available at ScienceDirect

Separation and Purification Technology

journal homepage: www.elsevier.com/locate/seppur

α-MnO_2/Palygorskite composite as an effective catalyst for heterogeneous activation of peroxymonosulfate (PMS) for the degradation of Rhodamine B

Chun Huang[a], Yulan Wang[a], Miao Gong[a], Wei Wang[a,*], Yang Mu[b], Zhen-Hu Hu[a,*]

[a] School of Civil Engineering, Hefei University of Technology, Hefei 230009, China
[b] Department of Chemistry, University of Science & Technology of China, Hefei 230026, China

ARTICLE INFO

Keywords:
α-MnO_2/Palygorskite
Peroxymonosulfate
RhB degradation
Mineralization

ABSTRACT

The discharging of Rhodamine B (RhB) from wastewater has caused huge environment pollution. Peroxymonosulfate (PMS) oxidation is an effective way to remove it from wastewater. However, finding an environmentally friendly metal to activate PMS is a key step for the oxidation process. In this study, nanorod α-MnO_2 loaded palygorskite (α-MnO_2/Pal) was fabricated by a simple hydrothermal method. The analysis of field emission scanning electron microscope (FE-SEM), X-ray diffraction (XRD), and X-ray photoelectron spectroscopy (XPS) confirmed the loading of α-MnO_2 on the surface of Pal and characterized the surface of the composite. The surface area of α-MnO_2/Pal composite was 159.13 m^2/g, which was much higher than that of Pal and α-MnO_2. The Pal, α-MnO_2, Mn^{2+}, and α-MnO_2/Pal were used to activate PMS for RhB degradation. Nearly 100% RhB degradation was obtained in α-MnO_2/Pal + PMS system in 180 min and in α-MnO_2 + PMS system in 300 min, while only 50% degradation was obtained in Pal + PMS system and 71.4% degradation in Mn^{2+} + PMS system in 300 min. The degradation fitted the pseudo-first-order reaction kinetics well with rate constant of 0.02041 min^{-1} for α-MnO_2/Pal + PMS system, 0.01192 min^{-1} for α-MnO_2 + PMS system, and 0.00435 min^{-1} for Mn^{2+} + PMS system, respectively. The factors affecting RhB degradation were further investigated. The RhB degradation efficiency increased with the increase of α-MnO_2/Pal dosages, PMS dosages and temperatures. The degradation was inhibited at pH > 5.5, while was favorable at pH < 5.5. The major reactive radicals responsible for RhB degradation classified by radical quenching experiment were $O_2^{\cdot -}$ and $^1O_2$. The possible mechanism was further proposed based on the results. The α-MnO_2/Pal composite showed nearly 50% mineralization ratio in the presence of PMS and an excellent reusability. The results from this study revealed that α-MnO_2/Pal composite is an effective catalyst to activate PMS for RhB degradation.

1. Introduction

Organic dyes discharged from printing, textile and leather industries have detrimental effects on the environment such as dark color and high chemical oxygen demand (COD) [1–3]. Rhodamine B (RhB) is a red dye and widely used in textiles dyeing, which is not only harmful to aquatic organisms, but also carcinogenic to humans and animals [4]. RhB is recalcitrant to biodegradation because of its complex structure [3,5]. Therefore, the physic-chemical treatment of RhB dye wastewater is a necessary way for controlling its pollution.

Researchers have tried many ways for addressing this problem such as coagulation/flocculation, activated carbon adsorption, membrane filtration and advanced oxidation processes (AOPs) [6–9]. Among these methods, AOPs using oxidizing agents such as H_2O_2, peroxymonosulfate (PMS) and O_3 have gained much attention because of the high efficiency and nonselective degradation [10–12]. Importantly, PMS can be activated by heating, UV irradiation, transition metallic oxide and so on [13,14]. Among these activation methods, the transition metal activation is the most suitable one because of its low energy consumption and the simplicity of the activation [15]. Cobalt-based materials have been investigated for activating peroxymonosulfate (PMS) [16,17], but they inevitably cause secondary heavy metal contamination because of the release of cobalt [18]. Therefore, it is very important to find an environmentally friendly metal to activate PMS.

Recently, manganese-based materials have been identified as promising heterogeneous catalysts for activating PMS due to its low cost, high stability, variable valence and high abundance in nature [14,19]. The electron transfer with oxidation state change (Mn^{2+}/Mn^{4+}) in manganese-based materials presents a superior potential as active sites for activating PMS [20]. Moreover, MnO_2 has different morphologies

* Corresponding authors.
E-mail addresses: dwhit@126.com (W. Wang), zhhu@hfut.edu.cn (Z.-H. Hu).

https://doi.org/10.1016/j.seppur.2019.115877
Received 7 July 2019; Received in revised form 30 July 2019; Accepted 1 August 2019
Available online 01 August 2019
1383-5866/

and structures such as α-MnO_2, β-MnO_2, and γ-MnO_2 with different behaviors in PMS-based oxidation [21]. Deng et al. used α-MnO_2 to activate PMS and reached nearly 94% ciprofloxacin degradation within 60 min [22]. Chen et al. obtained 98% RhB degradation within 15 min in the MnO_2/$MnFe_2O_4$ + PMS system [23]. Ghanbari et al. found that 100% 4-chlorophenol degradation occurred at 30 min combining MnO_2/UV with PMS [24]. Huang et al. reported that 100% phenol removal was obtained at 40 min over Cu-MnO_2 and PMS [25]. However, MnO_2 particles are prone to aggregation, which leads to a dramatically decrease in surface area, accessible active sites and catalytic efficiency [26]. The effective way to keep the dispersibility and catalytic efficiency is to load manganese dioxide particles on a stable support [27].

Palygorskite (Pal) is a crystalline hydrated magnesia-aluminosilicate clay mineral with lamellar structure and large surface area [28,29]. Pal could prevent metal oxides from agglomeration and make metal oxides exposing more active sites on the surface, which can improve catalytic activities [30]. Moreover, the large surface area of Pal could enhance the adsorption ability [1]. The coating of hybrid nanostructures of MnO_2 particles on Pal might combine the adsorption ability and the catalytic property together.

In this study, α-MnO_2/Pal composite was fabricated via a hydrothermal method. The composite was characterized by field emission scanning electron microscope (FE-SEM), X-ray diffraction (XRD), X-ray photoelectron spectroscopy (XPS), energy dispersive spectrometer (EDS) and N_2 physisorption. The prepared α-MnO_2/Pal composite was examined to activate PMS for the degradation of RhB in aqueous solution. The factors, such as catalyst dosages, PMS dosages, initial pH and temperatures on the activation were investigated. The degradation mechanisms were also explored. To the best of our knowledge, α-MnO_2/Pal composite is the first time to be tested in activating PMS.

2. Experimental section

2.1. Chemicals and reagents

Palygorskite (Pal) was purchased from Shandong Yousuo Chemical Technology Co., Ltd. Potassium monopersulfate triple salt ($KHSO_5{\cdot}0.5KHSO_4{\cdot}0.5K_2SO_4$, PMS) was purchased from Aladdin Chemistry Co., Ltd. Rhodamine B (RhB) was supplied by Shanghai Xinliang Chemical Reagent Co., LTD. Potassium permanganate ($KMnO_4$), hydrochloric acid (HCl, 37 wt%), sodium hydroxide (NaOH), sodium sulfite anhydrous (Na_2SO_3), ethanol (EtOH), triethylenediamine hexahydrate (DABCO) and p-Benzoquinone (p-BQ) were obtained from Sinopharm Chemical Reagent Co., Ltd. Manganese chloride ($MnCl_2{\cdot}4H_2O$) was obtained from Tianjin Guangfu Fine Chemical Research Institute. All the chemicals were used without further purification.

2.2. Catalyst preparation

In a typical procedure, 0.3656 g $KMnO_4$ and 0.8125 mL HCl were dissolved in ultrapure water (65 mL) under magnetic stirring to form the precursor solution. Then 0.5 g of Pal was added to the solution. After stirring for 20 min, the mixture was transferred into a 100 mL Teflon-lined stainless-steel autoclave. The autoclave was sealed and put into an oven at 150 °C for 8 h. Afterwards, the autoclave was taken out and naturally cooled down to room temperature. The precipitate was collected and washed with ultrapure water for five times. Finally, the product was harvested after cold drying with freeze dryer overnight. α-MnO_2 was also synthesized by a similar procedure as described above in the absence of Pal.

2.3. Experimental setup

The experiment consisted of the following five parts. Firstly, the adsorption property of Pal, α-MnO_2 and α-MnO_2/Pal were investigated, which was performed in the absence of PMS. Secondly, the degradation of RhB by Pal, α-MnO_2, Mn^{2+}, and α-MnO_2/Pal was compared. Thirdly, the factors affecting the degradation of RhB by α-MnO_2/Pal composite, such as catalyst dosages, PMS dosages, initial pH and temperatures, were investigated, in which the catalyst dosages and PMS dosages ranged from 0.01 g/L to 0.20 g/L, initial pH from 3.0 to 9.0 and temperatures from 10 °C to 40 °C, respectively. The initial pH of solution was adjusted by 1 M HCl or 1 M NaOH to the desired value. When investigating the effect of temperature, the desired temperature was heated through a water bath heater. As for 10 °C, a winter day with ambient temperature 10 °C was employed. Fourthly, three selective quenching agents, ethanol (EtOH), p-Benzoquinone (p-BQ) and triethylenediamine hexahydrate (DABCO) [14,31,32], were employed to assess the major reactive radicals responsible for RhB degradation. Lastly, the reusability and stability of α-MnO_2/Pal composite were tested. The composite was regenerated by filtration and washing with ultrapure water for five times after each reaction. Then the washed catalyst was dried in a freeze dryer overnight. The reaction solutions were collected after each run to detect the concentration of leaching Mn^{2+}. The experiments were repeated twice to ensure accuracy.

The experiment was carried out at room temperature (T = 20 ± 3 °C) in a 250 mL beaker containing 200 mL RhB aqueous solution with vigorous stirring. A stock solution (100 mg/L) of RhB was prepared and diluted to the required concentrations when necessary. At pre-determined time intervals, 1 mL liquid was withdrawn and filtered via a 0.45 μm Millipore filter, and the filtered solution was collected into a centrifuge tube, in which 2 mL 50 mM Na_2SO_3 was added in advance to quench the reaction [33].

2.4. Analytical methods

The micro-structure and chemical compositions of the catalyst were examined by field emission scanning electron microscope (FE-SEM, SU8020, Japan) equipped with an energy dispersive spectrometer (EDS). The crystalline structures of the catalyst were analyzed by an X-ray diffraction (XRD, X'Pert PRO MPD, Panaco, Netherlands) with Cu Kα radiation, operating at an accelerating voltage of 40 kV and current of 40 mA, respectively. The surface compositions and oxidation states of the catalysts were measured by X-ray photoelectron spectroscopy (XPS, Thermo escalab 250Xi). The specific surface area and pore size distribution were analyzed by N_2 adsorption/desorption at −196 °C using a physical adsorption analyzer (Autosorb-iQ, Quantachrome). The Brunauer-Emmett-Teller (BET) specific surface area was calculated with BET equation. The pore size distribution was obtained using the Barret-Joyner-Halenda (BJH) model [34].

The concentration of RhB was determined by a UV–vis spectrophotometer (Lambda 25, Perkin Elmer, America) at 554 nm [35]. The mineralization degree of RhB was measured by a TOC analyzer (TOC-V_{CPN}, Shimadzu Co., Ltd., Japan). The Mn^{2+} concentration was analyzed by inductively coupled plasma (ICP, Optima5300DV, PerkinElmer).

3. Results and discussion

3.1. Characterization of the catalysts

The morphology and microstructure of Pal, α-MnO_2, and α-MnO_2/Pal were characterized by FE-SEM. As shown in Fig. 1a, Pal consisted of planar fibers and some fibers formed agglomerated cluster, while α-MnO_2 showed the uniformly nanorods with a tunnel structure (Fig. 1b). As seen in Fig. 1c, the surface of the α-MnO_2/Pal composite was rough and densely porous. Plenty of rod-like particles were observed on the surface of α-MnO_2/Pal (Fig. 1d), indicating that the prepared α-MnO_2 was assembled on the surface of Pal. Furthermore, the EDS analysis further confirmed the loading of α-MnO_2 on the surface of Pal, as shown in Fig. 1e.

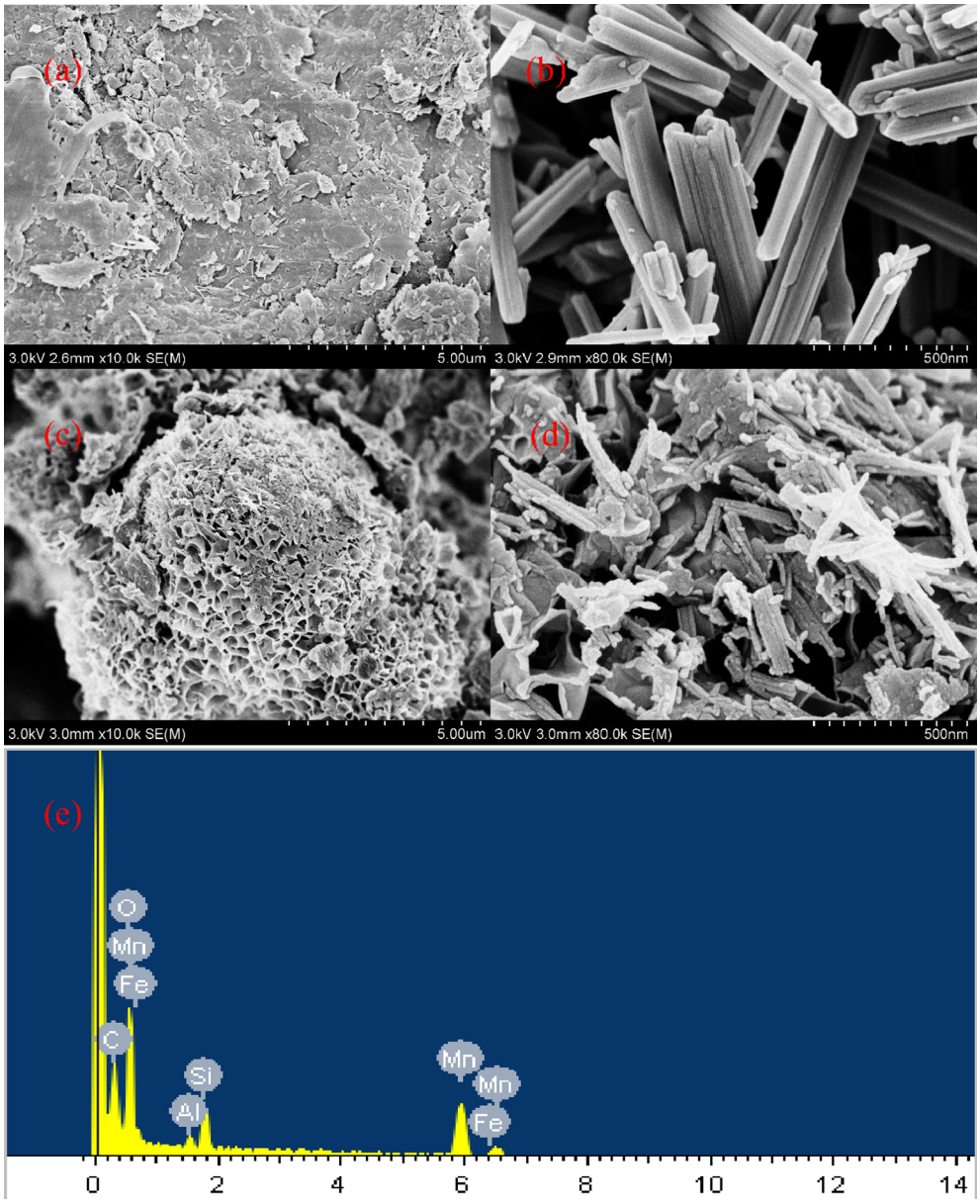

Fig. 1. SEM images of (a) Pal, (b) α-MnO_2, (c) and (d) α-MnO_2/Pal; and (e) EDS spectrum of α-MnO_2/Pal.

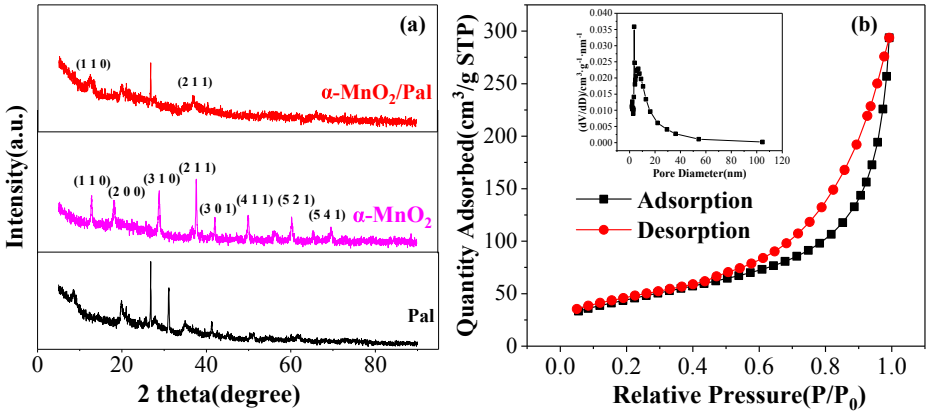

Fig. 2. (a) XRD patterns of Pal, α-MnO_2 and α-MnO_2/Pal; (b) N_2 sorption isotherms curve of α-MnO_2/Pal. Inset is the pore distribution of α-MnO_2/Pal.

The crystalline structures were examined by X-ray diffraction (XRD) patterns, as shown in Fig. 2a. The peak appeared at 2θ = 8.49° was corresponded to the crystalline Pal [28,36]. The characteristic diffraction peaks at 2θ = 13.91°, 16.46°, 19.89°, and 20.35° demonstrated the presence of Si-O-Si crystalline layer in the Pal [28]. The diffraction peaks found at 2θ of 12.78°, 18.11°, 28.84°, 37.52°, 41.97°, 49.86°, 60.27°, and 69.71° were well in agreement with the α-MnO_2 structure in the space group 14/m (JCPDS NO. 44-0141). These peaks could be indexed to (1 1 0), (2 0 0), (3 1 0), (2 1 1), (3 0 1), (4 1 1), (5 2 1) and (5 4 1), respectively [21,37]. For the α-MnO_2/Pal composite, the diffraction peaks of α-MnO_2 and Pal were more or less weakened, but the characteristic peaks at 12.78° and 37.52° (α-MnO_2) could be found, implying the successful synthesis. Nevertheless, the characteristic peaks of Pal were not detected in the α-MnO_2/Pal composite due to the poor crystallinity of α-MnO_2 [38].

To evaluate surface area and the pore size distribution, the α-MnO_2/Pal composite was examined by N_2 adsorption/desorption measurements, as shown in Fig. 2b. Based on the IUPAC classification, the composite demonstrated a type IV isotherm with a type H3 hysteresis loop, showing a representative mesoporous structure [20,34]. As shown in Fig. 2b, α-MnO_2/Pal showed a board hysteresis loop at a relative pressure (P/P_0) ranged from 0.46 to 0.99. Besides, the inset in Fig. 2b presented a narrow pore size distribution of the composite at 2–20 nm, which could be calculated by the Barret-Joyner-Halenda (BJH) model. The textural properties of Pal, α-MnO_2 and α-MnO_2/Pal, such as BET surface area, pore volume and average pore diameter were listed in Table 1. The surface areas of Pal, α-MnO_2, and α-MnO_2/Pal were 81.59, 10.41 and 159.13 m^2/g, respectively. Obviously, the synthesized α-MnO_2/Pal composite had a much higher BET surface area as compared to α-MnO_2, which could be attributed to the α-MnO_2/Pal composite was densely porous. The larger BET surface area and pore volume might improve the catalytic properties by providing more active sites and enhancing adsorption ability [1,27,34].

3.2. Adsorption and degradation of RhB

The adsorption and degradation of RhB by Pal, α-MnO_2, Mn^{2+}, and α-MnO_2/Pal were investigated to examine the property of catalyst. The adsorption property was tested by adding Pal, α-MnO_2, or α-MnO_2/Pal alone without PMS addition. As shown in Fig. 3a, the Pal or α-MnO_2 played a negligible role in the adsorption processes. However, the α-MnO_2/Pal composite exerted significant 50% RhB adsorption removal, which can be ascribed to the large BET surface area [1,39].

The degradation of RhB by Pal, α-MnO_2, Mn^{2+}, and α-MnO_2/Pal through activating PMS was further investigated using PMS alone as control. As shown in Fig. 3a, the oxidation efficiency of RhB was very limited with PMS alone, indicating that RhB could not be degraded well by PMS self-activation [40]. About 50% was degraded with the addition of Pal and PMS simultaneously after 300 min reaction, indicating that Pal has a certain catalytic capacity. α-MnO_2 and α-MnO_2/Pal composite showed nearly 100% RhB removal, and α-MnO_2/Pal needed shorter time as compared with α-MnO_2 alone, as shown in Fig. 3a, which might be because α-MnO_2/Pal combined the adsorption features and the catalytic properties together. Only 71.4% RhB degradation was achieved in Mn^{2+} + PMS system in 300 min, whose degradation efficiency was much lower than α-MnO_2/Pal + PMS system. This indicated that the α-MnO_2/Pal heterogeneous catalyst had better activity than the homogenous Mn^{2+}.

Table 1
The textural properties of Pal, α-MnO_2, and α-MnO_2/Pal.

	Surface area (S_{BET}, m^2/g)	Pore volume (cm^3/g)	Average pore diameter (nm)
Pal	81.59	0.1659	7.989
α-MnO_2	10.41	0.0496	21.680
α-MnO_2/Pal	159.13	0.4323	9.975

For comparing the degradation reaction kinetics, a pseudo-first-order reaction kinetics model (Eq. (1)) was used to describe the RhB degradation.

$$\mathrm{In}\left(\frac{C}{C_0}\right) = -kt \quad (1)$$

where C is the concentration of RhB at time t, C_0 is the initial RhB concentration and k is the pseudo-first-order rate constants.

The RhB degradation fitted the pseudo-first-order reaction kinetics model well, as shown in Fig. 3b. As shown in Fig. 3a, the RhB degradation efficiency was 71.4% in Mn^{2+} + PMS system in 300 min, while the RhB was completely degraded in 300 min in α-MnO_2 + PMS system and the time was reduced to 180 min in α-MnO_2/Pal + PMS system. Correspondingly, the pseudo-first-order rate constant was 0.00435 min^{-1} for Mn^{2+} + PMS system, 0.01192 min^{-1} for α-MnO_2 + PMS system and 0.02041 min^{-1} for α-MnO_2/Pal + PMS system, further confirming the enhancement of α-MnO_2/Pal catalytic property. It could be attributed to the high adsorption ability and the more active sites on the surface [34].

3.3. Factors affecting degradation of RhB by α-MnO_2/Pal composite

RhB was effectively degraded by α-MnO_2/Pal composite. The effect of factors such as catalyst dosage, PMS concentration, initial pH and temperature on the degradation was further investigated.

Fig. 4a shows the effect of catalyst dosage on the RhB degradation. The degradation efficiency of RhB increased with the increasing catalyst dosage. The degradation efficiency of RhB increased from 38% to 83% in 300 min with the increase of catalyst dosage from 0.01 g/L to 0.05 g/L. The complete degradation of RhB was achieved at 180 min at the catalyst concentration of 0.10 g/L, which was further decreased to 60 min with the catalyst concentration increasing to 0.20 g/L. These results might be because more active sites were provided with increasing catalyst concentration [1,23].

The oxidant concentration was also of great importance on target pollutant removal. Fig. 4b shows the degradation efficiency of RhB at various PMS concentrations. The degradation efficiency of RhB increased with the increase of PMS from 0.01 g/L to 0.20 g/L. It can be explained that more oxidative radicals were produced with the increasing PMS concentration, enhancing the degradation efficiency [1,23].

The oxidative radical production was also affected by pH. The RhB degradation efficiency at different initial pH (pH = 3.0, 5.5, 7.0, and 9.0) was investigated. As shown in Fig. 4c, RhB had high oxidation efficiency at pH < 5.5, while the oxidation efficiency obviously decreased when the pH > 5.5. The main reason for this phenomenon might be because PMS was unstable and generated non-radicals under alkaline conditions (Eq. (2)) [41,42], resulting in a drastic decrease of oxidation efficiency.

$$HSO_5^- + OH^- \rightarrow SO_4^{2-} + \frac{1}{2}O_2 + H_2O \quad (2)$$

Temperature is also an important factor affecting oxidation efficiency [34]. The RhB degradation was examined at different temperature. As seen in Fig. 4d, the time for 100% RhB degradation decreased dramatically from 300 min to 60 min when the temperature increased from 10 °C to 40 °C. All of these reactions fitted the pseudo-first-order reaction kinetics well, and the pseudo-first-order rate constants were listed in Table 2. By drawing the In k against 1/T (inset of Fig. 4d) based on the Arrhenius equation, activation energy (E_a) of the catalyst was calculated as 38.283 kJ/mol, which were intrinsically similar to other Mn-based materials [34].

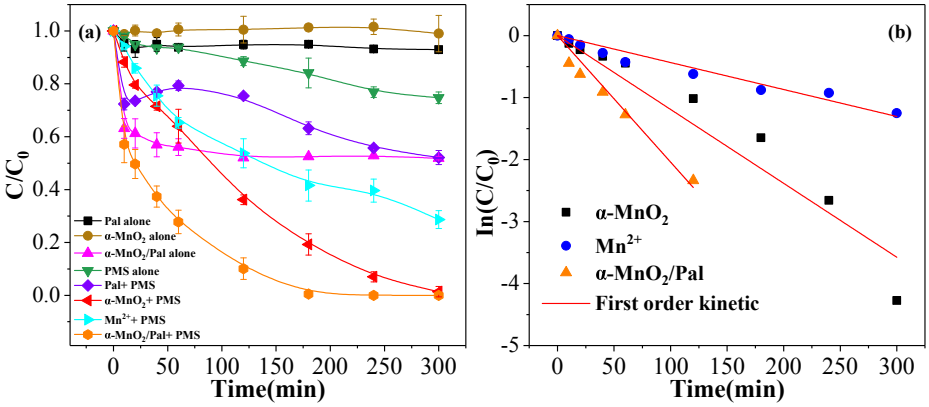

Fig. 3. (a) Adsorption and degradation of RhB under various conditions, and (b) first order kinetic model of degradation reactions. Experimental conditions: $[RhB]_0$ = 20 mg/L, catalyst loading = 0.10 g/L, PMS loading = 0.10 g/L, pH = (5.5 ± 0.1), and temperature = 20 °C.

3.4. Mineralization analysis of RhB degradation

The mineralization was also investigated based on the change of total organic carbon (TOC) value. The contribution of adsorption on the TOC removal was first investigated with the only addition of Pal, α-MnO_2, or α-MnO_2/Pal. As shown in Fig. 5a, the RhB adsorption removal by Pal, α-MnO_2 and α-MnO_2/Pal was 15.3%, 4.8% and 25.0%, respectively. After RhB degradation under different reaction systems, the variation of TOC was further analyzed. As shown in Fig. 5b, the mineralization efficiency reached 4.3% in the PMS alone, 18.9% in the Pal + PMS system, 10.5% in the Mn^{2+} + PMS system, 53.2% in the α-MnO_2 + PMS system, and 51.2% in the α-MnO_2/Pal + PMS system, indicating a favorable RhB mineralization under the latter two systems. These results indicated that α-MnO_2 and α-MnO_2/Pal composite had higher catalytic ability. Interestingly, the degradation efficiency of RhB achieved 100% within 5 h, but the mineralization ratio was only 51.2%. These phenomena can be due to the intermediate products being produced during the degradation process [19].

3.5. Mechanism of PMS activation by α-MnO_2/Pal

To acquire the major responsible reactive radicals for RhB degradation, radical quenching tests were carried out by using ethanol (EtOH), p-Benzoquinone (p-BQ) and triethylenediamine hexahydrate (DABCO) as quenching agents. EtOH could sufficiently quench both $SO_4^{\cdot -}$ and ·OH with the first-order reaction rate constant of 1.6–7.7 × 10^7 M^{-1} s^{-1} for $SO_4^{\cdot -}$ and 1.2–2.8 × 10^9 M^{-1} s^{-1} for ·OH [14]. p-BQ is a scavenger of superoxide radical ($O_2^{\cdot -}$) with the first-order reaction rate constant of 9.6 × 10^8 M^{-1} s^{-1} [31,43]. The singlet oxygen ($^1O_2$) is inhibited by DABCO with the first-order reaction rate constant of 2.8 × 10^8 M^{-1} s^{-1} [32,44,45]. Therefore, the dominant radical species for RhB degradation could be differentiated by the addition of EtOH, p-BQ or DABCO into the reaction solution. As shown in Fig. 6a, when 3 mM EtOH was added, the degradation trend of RhB was similar to the control group, suggesting that $SO_4^{\cdot -}$ and ·OH were not

Table 2
Kinetics of RhB degradation at different temperature by α-MnO_2/Pal catalyst.

T (°C)	K (min^{-1})	R^2 of k	E_a (kJ/mol)	R^2 of E_a
10	0.0151	0.985	38.283	0.961
20	0.0204	0.985		
30	0.0368	0.997		
40	0.0723	0.998		

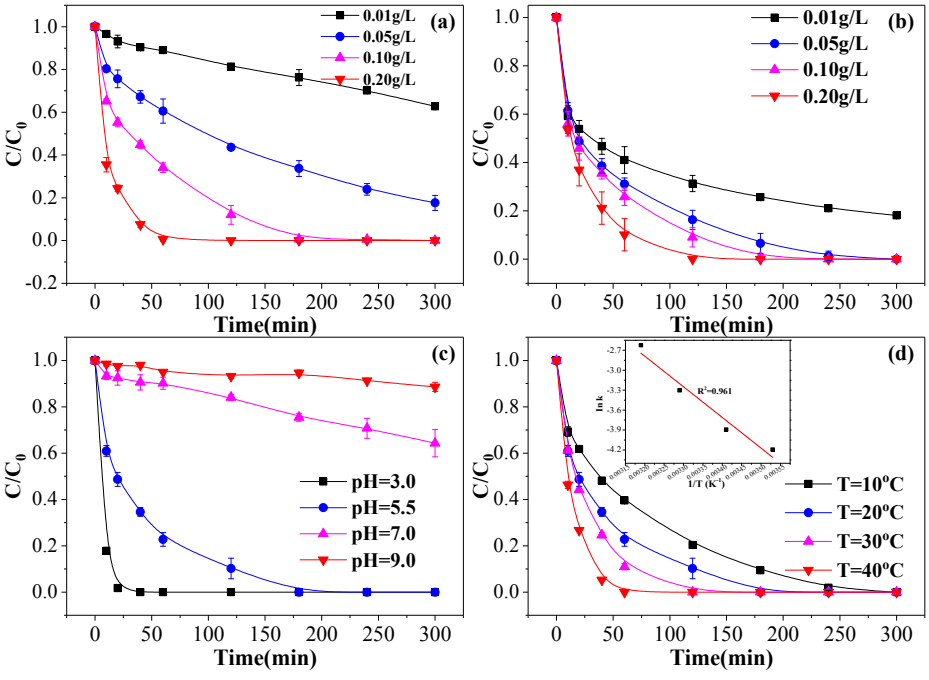

Fig. 4. The factors affecting RhB degradation by α-MnO_2/Pal composite: (a) catalyst dosage, (b) PMS concentration, (c) initial pH, and (d) temperature. General experimental conditions: (a) $[RhB]_0$ = 20 mg/L, PMS loading = 0.10 g/L, pH = (5.5 ± 0.1), temperature = 20 °C, (b) $[RhB]_0$ = 20 mg/L, catalyst loading = 0.10 g/L, pH = (5.5 ± 0.1), temperature = 20 °C, (c) $[RhB]_0$ = 20 mg/L, catalyst loading = 0.10 g/L, PMS loading = 0.10 g/L, temperature = 20 °C, (d) $[RhB]_0$ = 20 mg/L, catalyst loading = 0.10 g/L, PMS loading = 0.10 g/L, pH = (5.5 ± 0.1).

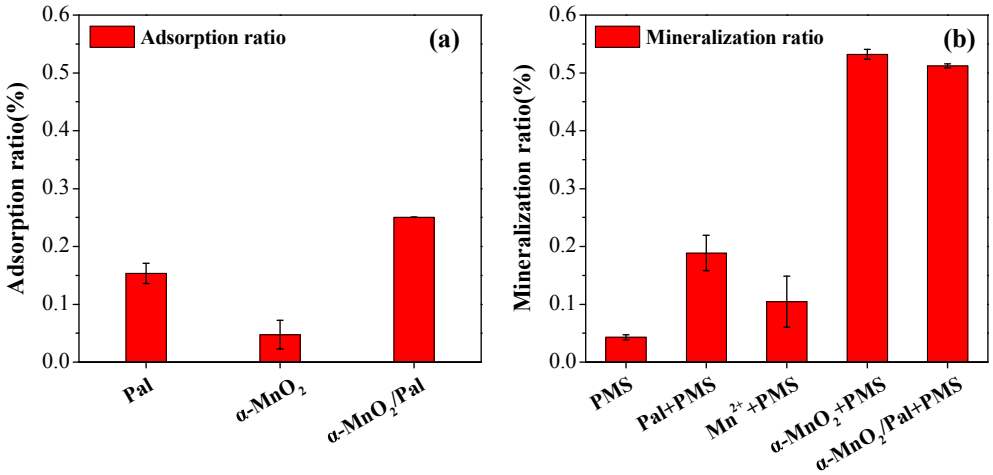

Fig. 5. (a) RhB adsorption and (b) mineralization ratio at different reaction systems. Experimental conditions: $[RhB]_0$ = 20 mg/L, catalyst loading = 0.10 g/L, PMS loading = 0.10 g/L, pH = (5.5 ± 0.1), T = 5 h, temperature = 20 °C.

the major radical species responsible for RhB degradation. On the contrast, when 3 mM p-BQ was added, the degradation efficiency of RhB under identical conditions was decreased from 100% to 75%, indicating that $O_2^{\cdot -}$ was involved in the reaction system. In addition, the RhB degradation was almost inhibited in the presence of 3 mM DABCO, suggesting that $^1O_2$ played an important role in the reaction system. These results illustrated that both $O_2^{\cdot -}$ and $^1O_2$ were the dominant reactive radicals in the PMS + α-MnO_2/Pal system.

To further understand the activation mechanism of PMS by α-MnO_2/Pal, XPS was employed to determine the near-surface chemical states of α-MnO_2/Pal. The valence states of manganese oxides in composite before and after oxidation were measured, as shown in Fig. 6b. The two high-resolution spectra peaks appeared at 641.7 eV and 642.9 eV in the Mn, $2p_{3/2}$ core region indicated the presence of Mn (III) and Mn (IV), respectively [46,47]. The relative contributions to the Mn (III) and Mn (IV) intensity were 26.9% and 73.1%, respectively. Two characteristic peaks appeared at 642.3 eV and 653.5 eV in the Mn 2p region represented Mn $2p_{3/2}$ and Mn $2p_{1/2}$. And the spin energy separation of 11.2 eV was a typical value for MnO_2 [20,48]. As seen in Fig. 6b, after the reaction, the relative contribution of Mn (III) increased from 26.9% to 72.3%, while Mn (IV) contribution decreased from 73.1% to 27.7%. The transformation from Mn (IV) to Mn (III) illustrated that the metal species transformation of α-MnO_2/Pal during PMS activation [49–51]. Based on the results of previous studies and radicals quenching experiments discussed above, the mechanism of α-MnO_2/Pal activation PMS degradation of RhB can be proposed as follows [23,46,52–56]:

$$\equiv Mn(IV) + HSO_5^- \rightarrow \equiv Mn(III) + SO_5^{\cdot -} + H^+ \quad (3)$$

$$\equiv Mn(III) + HSO_5^- \rightarrow \equiv Mn(IV) + SO_4^{\cdot -} + OH^- \quad (4)$$

$$HSO_5^- + H_2O \rightarrow H_2O_2 + HSO_4^- \quad (5)$$

$$SO_4^{\cdot -} + OH^- \rightarrow SO_4^{2-} + \cdot OH \quad (6)$$

$$H_2O_2 + \cdot OH \rightarrow HO_2^{\cdot} + H_2O \quad (7)$$

$$HO_2^{\cdot} \rightarrow H^+ + O_2^{\cdot -} \quad (8)$$

$$O_2^{\cdot -} + \cdot OH \rightarrow {}^1O_2 + OH^- \quad (9)$$

$$O_2^{\cdot -} + O_2^{\cdot -} + 2H^+ \rightarrow {}^1O_2 + H_2O_2 \quad (10)$$

$$HSO_5^- + SO_5^{2-} \rightarrow HSO_4^- + SO_4^{2-} + {}^1O_2 \quad (11)$$

3.6. Reusability and stability of the catalyst

It is essential to evaluate reusability of α-MnO_2/Pal catalyst, and three-run recyclability tests were done in this work. As shown in Fig. 7, it was clearly found that the RhB degradation via PMS activated by α-MnO_2/Pal decreased from 100% (first run) to 91% (second run) and 94% (third run). In the cyclic experiments nearly 91% RhB was removed within 300 min. The degradation efficiency of RhB decreased in the cyclic experiment of catalyst was probably due to the adsorption of the reaction intermediates on the surface of the catalyst [21]. The similar deactivation of the catalyst in the second and third run suggested

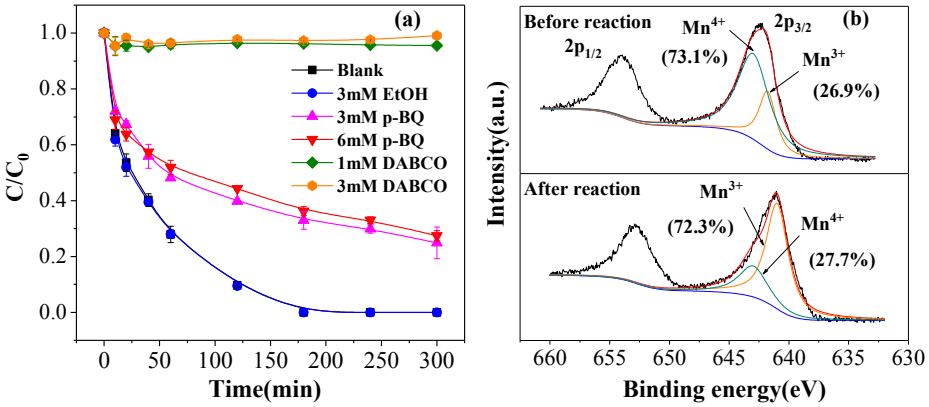

Fig. 6. (a) Influence of quenching agents on the degradation efficiency of RhB. Experimental conditions: $[RhB]_0$ = 20 mg/L, catalyst loading = 0.10 g/L, PMS loading = 0.10 g/L, pH = (5.5 ± 0.1), and temperature = 20 °C. (b) XPS spectra of Mn 2p before and after reaction for the α-MnO_2/Pal composite.

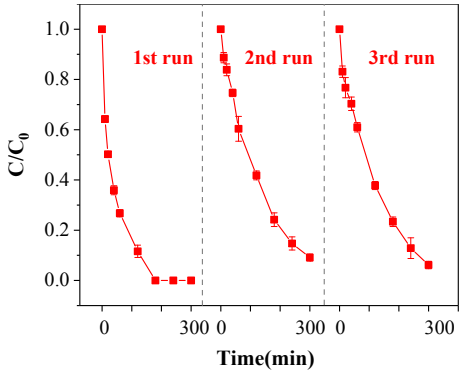

Fig. 7. Reusability tests of α-MnO_2/Pal for RhB degradation. Experimental conditions: $[RhB]_0$ = 20 mg/L, catalyst loading = 0.10 g/L, PMS loading = 0.10 g/L, pH = (5.5 ± 0.1), and temperature = 20 °C.

that the adsorbed intermediates could not be removed by simple filtration and water washing. It was found that 0.447 mg/L Mn^{2+} leaching in the first run, 0.456 mg/L in the second run, and 0.493 mg/L in the third run, indicating the good stability of the α-MnO_2/Pal composite. In a word, it can be said that the prepared catalyst still possesses good catalytic activity within three recycle cycles, which was important in pragmatic applications.

4. Conclusions

In this study, α-MnO_2/Pal composites were synthesized by hydrothermal method. The analysis of FE-SEM, EDS and XRD confirmed the successful loading of α-MnO_2 on Pal. The surface area of α-MnO_2/Pal was 159.13 m^2/g, which was much higher than that of Pal and α-MnO_2. The 20 mg/L RhB degradation efficiency reached as high as 100% within 180 min at the conditions of 0.10 g/L α-MnO_2/Pal and 0.10 g/L PMS. The degradation fitted the pseudo-first-order reaction kinetics well with the rate constant of 0.02041 min^{-1}. The degradation efficiency increased with the increase of α-MnO_2/Pal dosages, PMS dosages and temperatures. The degradation was inhibited at pH > 5.5, while was favorable at pH < 5.5. The highest 51.2% of RhB was mineralized by PMS activated by α-MnO_2/Pal composite. The dominated radicals for RhB degradation were $O_2^{\cdot -}$ and $^1O_2$. Recycling tests showed that α-MnO_2/Pal composites possessed an excellent stability even after three successive runs. In summary, the synthesized α-MnO_2/Pal composite exhibited remarkable efficiency compared with either raw Pal or α-MnO_2 in activating PMS to degrade RhB.

Acknowledgements

This research was partially supported by the Science and Technology Major Project of Anhui Province (18030801102). And the National Natural Science Foundation of China (Grant No. 51728801, 51578205, 51538012).

References

[1] F. Ji, C.L. Li, X.Y. Wei, J. Yu, Efficient performance of porous Fe2O3 in heterogeneous activation of peroxymonosulfate for decolorization of Rhodamine B, Chem. Eng. J. 231 (2013) 434–440.
[2] H.-Y. Shu, M.-C. Chang, Decolorization and mineralization of a phthalocyanine dye C.I. Direct Blue 199 using UV/H2O2 process, J. Hazard. Mater. 125 (1–3) (2005) 96–101.
[3] M.X. Zhu, L. Li, H.H. Wang, Z. Wang, Removal of an anionic dye by adsorption/precipitation processes using alkaline white mud, J. Hazard. Mater. 149 (2007) 735–741.
[4] C. Lops, A. Ancona, K. Di Cesare, B. Dumontel, N. Garino, G. Canavese, S. Hérnandez, V. Cauda, Sonophotocatalytic degradation mechanisms of Rhodamine B dye via radicals generation by micro- and nano-particles of ZnO, Appl. Catal. B Environ. 243 (2019) 629–640.
[5] H. Fu, C. Pan, W. Yao, Y. Zhu, Visible-light-induced degradation of rhodamine B by nanosized Bi2WO6, J. Phys. Chem. B 109 (2005) 22432–22439.
[6] G. Han, C.Z. Liang, T.S. Chung, M. Weber, C. Staudt, C. Maletzko, Combination of forward osmosis (FO) processwith coagulation/flocculation (CF) for potential treatment of textile wastewater, Water Res. 91 (2016) 361–370.
[7] C. Grégorio, Non-conventional low-cost adsorbents for dye removal: a review, Bioresour. Technol. 97 (2006) 1061–1085.
[8] H.P. Ngang, B.S. Ooi, A.L. Ahmad, S.O. Lai, Preparation of PVDF–TiO 2 mixed-matrix membrane and its evaluation on dye adsorption and UV-cleaning properties, Chem. Eng. J. 197 (2012) 359–367.
[9] W. Zhang, H.L. Tay, S.S. Lim, Y.S. Wang, Z.Y. Zhong, R. Xu, Supported cobalt oxide on MgO: highly efficient catalysts for degradation of organic dyes in dilute solutions, Appl. Catal. B Environ. 95 (2010) 93–99.
[10] H.W. Liang, H.Q. Sun, A. Patel, P. Shukla, Z.H. Zhu, S.B. Wang, Excellent performance of mesoporous Co3O4/MnO2 nanoparticles in heterogeneous activation of peroxymonosulfate for phenol degradation in aqueous solutions, Appl. Catal. B Environ. 127 (2012) 330–335.
[11] I.A. Alaton, I.A. Balcioglu, D.W. Bahnemann, Advanced oxidation of a reactive dyebath effluent: comparison of O3, H2O2/UV-C and TiO2/UV-A processes, Water Res. 36 (2002) 1143–1154.
[12] N.N. Tusar, D. Maucec, M. Rangus, I. Arcon, M. Mazaj, M. Cotman, A. Pintar, V. Kaucic, Manganese functionalized silicate nanoparticles as a Fenton-type catalyst for water purification by Advanced Oxidation Processes (AOP), Adv. Funct. Mater. 22 (2012) 820–826.
[13] T. Zhang, H. Zhu, J.P. Croue, Production of sulfate radical from peroxymonosulfate induced by a magnetically separable CuFe2O4 spinel in water: efficiency, stability, and mechanism, Environ. Sci. Technol. 47 (2013) 2784–2791.
[14] X.S. Luo, H. Liang, F.S. Qu, A. Ding, X.X. Cheng, C.Y. Tang, G.B. Li, Free-standing hierarchical α-MnO2 @CuO membrane for catalytic filtration degradation of organic pollutants, Chemosphere 200 (2018) 237–247.
[15] Y. Leng, W. Guo, S. Xiao, Y. Li, A. Wang, F. Hao, L. Xing, Degradation of Rhodamine B by persulfate activated with Fe3O4: effect of polyhydroquinone serving as an electron shuttle, Chem. Eng. J. 240 (2014) 338–343.
[16] P. Shukla, H.Q. Sun, S.B. Wang, H.M. Ang, M.O. Tade, Nanosized Co3O4/SiO2 for heterogeneous oxidation of phenolic contaminants in waste water, Sep. Purif. Technol. 77 (2011) 230–236.
[17] R. Luo, C. Liu, J.S. Li, C.H. Wang, X.Y. Sun, J.Y. Shen, W.Q. Han, L.J. Wang, Convenient synthesis and engineering of ultrafine Co3O4-incorporated carbon composite: towards practical application of environmental remediation, J. Mater. Chem. A 6 (8) (2018) 3454–3461.
[18] P.D. Hu, M.C. Long, Cobalt-catalyzed sulfate radical-based advanced oxidation: a review on heterogeneous catalysts and applications, Appl. Catal. B Environ. 181 (2016) 103–117.
[19] H. Sun, Y.X. Shang, K.L. Xu, Y.N. Tang, J.Y. Li, Z.N. Liu, MnO2 aerogels for highly efficient oxidative degradation of Rhodamine B, RSC Adv. 7 (48) (2017) 30283–30288.
[20] Y.X. Wang, Y.B. Xie, H.Q. Sun, J.D. Xiao, H.B. Cao, S.B. Wang, 2D/2D nano-hybrids of γ-MnO2 on reduced graphene oxide for catalytic ozonation and coupling peroxymonosulfate activation, J. Hazard. Mater. 301 (2016) 56–64.
[21] S. Edy, M. Syaifullah, H.Q. Sun, H.M. Ang, M.O. Tadé, S.B. Wang, Different crystallographic one-dimensional MnO2 nanomaterials and their superior performance in catalytic phenol degradation, Environ. Sci. Technol. 47 (2013) 5882–5887.
[22] J. Deng, Y.J. Ge, C.Q. Tan, H.Y. Wang, Q.S. Li, S.Q. Zhou, K.J. Zhang, Degradation of ciprofloxacin using α-MnO2 activated peroxymonosulfate process: effect of water constituents, degradation intermediates and toxicity evaluation, Chem. Eng. J. 330 (2017) 1390–1400.
[23] G. Chen, X.Y. Zhang, Y.J. Gao, G.X. Zhu, Q.F. Cheng, X.W. Cheng, Novel magnetic MnO2/MnFe2O4 nanocomposite as a heterogeneous catalyst for activation of peroxymonosulfate (PMS) toward oxidation of organic pollutants, Sep. Purif. Technol. 213 (2019) 456–464.
[24] A. Eslami, M. Hashemi, F. Ghanbari, Degradation of 4-chlorophenol using catalyzed peroxymonosulfate with nano-MnO2/UV irradiation: toxicity assessment and evaluation for industrial wastewater treatment, J. Clean. Prod. 195 (2018) 1389–1397.
[25] Y.L. Huang, X.K. Tian, Y.L. Nie, C. Yang, Y.X. Wang, Enhanced peroxymonosulfate activation for phenol degradation over MnO2 at pH 3.5-9.0 via Cu(II) substitution, J. Hazard. Mater. 360 (2018) 303–310.
[26] Y.K. Yang, H. Zhang, S.G. Jin, A new method of activated carbon loading MnO2 to formaldehyde degradation, Adv. Mater. Res. 332–334 (2011) 1743–1746.
[27] D. Liu, C.R. Wang, Y.F. Song, Y.H. Wei, L. He, B.R. Lan, X.W. He, J.B. Wang, Effective mineralization of quinoline and bio-treated coking wastewater by catalytic ozonation using CuFe2O4/Sepiolite catalyst: efficiency and mechanism, Chemosphere 227 (2019) 647–656.
[28] E. Stathatos, D. Papoulis, C.A. Aggelopoulos, D. Panagiotaras, A. Nikolopoulou, TiO2/palygorskite composite nanocrystalline films prepared by surfactant templating route: Synergistic effect to the photocatalytic degradation of an azo-dye in water, J. Hazard. Mater. 211–212 (2012) 68–76.
[29] X.Z. Li, H.Y. Shi, W. Zhu, S.X. Zuo, X.W. Lu, S.P. Luo, Z.Y. Li, C. Yao, Y.S. Chen, Nanocomposite LaFe1-xNixO3/Palygorskite catalyst for photo-assisted reduction of NOx: effect of Ni doping, Appl. Catal. B Environ. 231 (2018) 92–100.
[30] X.Y. Li, K. Peng, Hydrothermal synthesis of MoS2 nanosheet/palygorskite nanofiber hybrid nanostructures for enhanced catalytic activity, Appl. Clay Sci. 162 (2018) 175–181.
[31] A. Jawad, X.Y. Lu, Z.Q. Chen, G.C. Yin, Degradation of chlorophenols by supported Co-Mg-Al layered double hydrotalcite with bicarbonate activated hydrogen peroxide, J. Phys. Chem. A 118 (2014) 10028–10035.
[32] M. Stylidi, D.I. Kondarides, X.E. Verykios, Visible light-induced photocatalytic degradation of Acid Orange 7 in aqueous TiO2 suspensions, Appl. Catal. B Environ. 47

(2004) 189–201.
[33] Q.-N. Liao, F. Ji, J.-C. Li, X.M. Zhan, Z.-H. Hu, Decomposition and mineralization of sulfaquinoxaline sodium during UV/H2O2 oxidation processes, Chem. Eng. J. 284 (2016) 494–502.
[34] Y.X. Wang, H.Q. Sun, H.M. Ang, M.O. Tadé, S.B. Wang, Facile synthesis of hierarchically structured magnetic MnO2/ZnFe2O4 hybrid materials and their performance in heterogeneous activation of peroxymonosulfate, ACS Appl. Mater. Inter. 6 (2014) 19914–19923.
[35] C. Xu, H. Wu, F.L. Gu, Efficient adsorption and photocatalytic degradation of Rhodamine B under visible light irradiation over BiOBr/montmorillonite composites, J. Hazard. Mater. 275 (2014) 185–192.
[36] X.H. Zou, T.H. Chen, H.B. Liu, P. Zhang, Z.Y. Ma, J.J. Xie, D. Chen, An insight into the effect of calcination conditions on catalytic cracking of toluene over 3Fe8Ni/palygorskite: catalysts characterization and performance, Fuel 190 (2017) 47–57.
[37] X. Wang, Y.D. Li, Synthesis and formation mechanism of manganese dioxide nanowires/nanorods, Chem. Eur. J. 9 (2003) 300–306.
[38] C. Song, B.-B. Guo, X.-F. Sun, S.-G. Wang, Y.-T. Li, Enrichment and degradation of tetracycline using three-dimensional graphene/MnO2 composites, Chem. Eng. J. 358 (2019) 1139–1146.
[39] B. Nanda, A.C. Pradhan, K.M. Parida, A comparative study on adsorption and photocatalytic dye degradation under visible light irradiation by mesoporous MnO 2 modified MCM-41 nanocomposite, Micropor. Mesopor. Mat. 226 (2016) 229–242.
[40] P. Liang, C. Zhang, X.G. Duan, H.Q. Sun, S.B. Wang, An insight to metal organic framework derived N-doped graphene towards oxidative degradation of persistent contaminants: generation of singlet oxygen from peroxymonosulfate, Environ. Sci. Nano 4 (2017) 315–324.
[41] F. Ghanbari, C.A. Martínez-Huitle, Electrochemical advanced oxidation processes coupled with peroxymonosulfate for the treatment of real washing machine effluent: a comparative study, J. Electroanal. Chem. 847 (2019) 113182.
[42] M. Ahmadi, F. Ghanbari, Organic dye degradation through peroxymonosulfate catalyzed by reusable graphite felt/ferriferrous oxide: mechanism and identification of intermediates, Mater. Res. Bull. 111 (2019) 43–52.
[43] J. Bandara, J. Kiwi, Fast kinetic spectroscopy, decoloration and production of H2O2 induced by visible light in oxygenated solutions of the azo dye Orange II, New J. Chem. 23 (1999) 717–724.
[44] Y.A. Lion, E. Gandin, A.V.D. Vorst, On the production of nitroxide radicals by singlet oxygen reaction: an EPR study, Photochem. Photobiol. 31 (1980) 305–309.
[45] J.Z. Meng, F. Xu, S.J. Yuan, Y. Mu, W. Wang, Z.-H. Hu, Photocatalytic oxidation of roxarsone using riboflavin-derivative as a photosensitizer, Chem. Eng. J. 355 (2019) 130–136.
[46] S.L. Luo, L. Duan, B.Z. Sun, M.Y. Wei, X.X. Li, A.H. Xu, Manganese oxide octahedral molecular sieve (OMS-2) as an effective catalyst for degradation of organic dyes in aqueous solutions in the presence of peroxymonosulfate, Appl. Catal. B Environ. 164 (2015) 92–99.
[47] Z. Tong, X. Yan, D.D. Sun, Hierarchically multifunctional K-OMS-2/TiO2/Fe3O4 heterojunctions for the photocatalytic oxidation of humic acid under solar light irradiation, J. Hazard. Mater. 243 (2012) 302–310.
[48] Z. Lei, F. Shi, L. Lu, Incorporation of MnO2-coated carbon nanotubes between graphene sheets as supercapacitor electrode, ACS Appl. Mater. Inter. 4 (2012) 1058–1064.
[49] D. Chen, X.L. Ma, J.Z. Zhou, X. Chen, G.R. Qian, Sulfate radical-induced degradation of Acid Orange 7 by a new magnetic composite catalyzed peroxymonosulfate oxidation process, J. Hazard. Mater. 279 (2014) 476–484.
[50] W. Zhang, H.L. Tay, S.S. Lim, Y.S. Wang, Supported cobalt oxide on MgO: highly efficient catalysts for degradation of organic dyes in dilute solutions, Appl. Catal. B Environ. 95 (2010) 93–99.
[51] J. Liu, Z. Zhao, P. Shao, F. Cui, Activation of peroxymonosulfate with magnetic Fe3O4–MnO2 core–shell nanocomposites for 4-chlorophenol degradation, Chem. Eng. J. 262 (2015) 854–861.
[52] C.D. Qi, X.T. Liu, J. Ma, C.Y. Lin, X.W. Li, H.J. Zhang, Activation of peroxymonosulfate by base: implications for the degradation of organic pollutants, Chemosphere 151 (2016) 280–288.
[53] F.G. Wang, W.J. Wang, S.J. Yuan, W. Wang, Z.-H. Hu, Comparison of UV/H2O2 and UV/PS processes for the degradation of thiamphenicol in aqueous solution, J. Photoch. Photobio. A 348 (2017) 79–88.
[54] M. Ahmadi, F. Ghanbari, Degradation of organic pollutants by photoelectro-peroxone/ZVI process: synergistic, kinetic and feasibility studies, J. Environ. Manage. 228 (2018) 32–39.
[55] M. Ahmadi, F. Ghanbari, Combination of UVC-LEDs and ultrasound for peroxymonosulfate activation to degrade synthetic dye: influence of promotional and inhibitory agents and application for real wastewater, Environ. Sci. Pollut. R. 25 (2018) 6003–6014.
[56] Y. Zhou, J. Jiang, Y. Gao, J. Ma, S.-Y. Pang, J. Li, X.-T. Lu, L.-P. Yuan, Activation of peroxymonosulfate by benzoquinone: a novel non-radical oxidation process, Environ. Sci. Technol. 49 (2015) 12941–12950.